SIN-CHN SCIENTIFIC PRESS PTE.LTD.

Molecular & Cellular Biomechanics 2025, 22(4), 1383.
https://doi.org/10.62617/mcb1383

Article

Optimization of helmet protection performance for soldiers' head protection on the battlefield

Yuanyuan Song[1,2,*], Zhuowei Chen[1,2]

[1] Institute of Urban Safety and Environmental Science, Beijing Academy of Science and Technology, Beijing 10054, China
[2] National Quality Testing Center for Personal Protective Equipment, Beijing 10054, China
*** Corresponding author:** Yuanyuan Song, 15110128820@163.com

CITATION

Song Y, Chen Z. Optimization of helmet protection performance for soldiers' head protection on the battlefield. Molecular & Cellular Biomechanics. 2025; 22(4): 1383. https://doi.org/10.62617/mcb1383

ARTICLE INFO

Received: 15 January 2025
Accepted: 19 February 2025
Available online: 4 March 2025

Abstract: Craniocerebral injury is one of the main causes of injury to soldiers in modern warfare, with explosive shock waves causing particularly severe damage to soldiers' heads. The research aims to optimize the protective performance of existing combat helmets through numerical simulation techniques, providing safer and more effective head protection equipment for soldiers on the battlefield. The Lagrange multiplier method is used to establish the numerical simulation model of explosion shock wave, and the finite element model of the head wearing combat helmet is created to analyze the defects of existing helmets under the explosion impact, so as to complete the optimization of the shape, material distribution and cushion foam structure of the helmet. The results show that wearing the new helmet results in a 36% lower incidence of traumatic brain injury compared to wearing traditional combat helmets. When polyurea material is used as the inner and outer double-sided layer, the deformation degree of the helmet material is the highest, and the shock wave energy absorption value is 23.5 J per impact. The results indicate that the optimized combat helmet significantly improves the explosion shock wave protection performance and reduces the risk of traumatic brain injury. The research results provide new ideas for the design of military protective equipment, which can enhance the survival ability of soldiers in complex battlefield environments.

Keywords: shock wave; craniocerebral injury; numerical simulation; helmet; protect

1. Introduction

With the increasingly complex modern battlefield environment, the scope of use of new weapons and equipment such as drones continues to expand, and precision guided missiles have become an important method for attackers to effectively preserve their own vital forces during attacks [1]. In this context, the proportion of traumatic brain injuries to soldiers caused by blast shockwaves has risen [2]. In the wars in Afghanistan and Iraq, data reported by the US military show that cranial brain injuries caused by blast shockwaves accounted for 30%–40% of all battlefield head injuries. Many soldiers suffered varying degrees of traumatic brain injury even though they wore traditional combat helmets [3]. Combat helmets are the core line of defense for protecting soldiers' heads, and their protective performance is extremely important for effectively protecting soldiers' lives and safety. The traditional design of combat helmets is mainly based on experiments, and the protective performance of helmets is improved through repeated experiments. However, this method not only has a long experimental cycle and consumes a significant amount of material costs, but also has the problem of difficulty in comprehensively evaluating the protective effect of helmets in complex explosive environments. As the computer

industry rapidly develops, three-dimensional numerical simulation technology (NST) has provided new possibilities for simulating real explosion scenes and analyzing shock states. Lagrange multiplier method is a mathematical optimization method that is particularly suitable for solving optimization problems with equality and inequality constraints [4]. The Lagrange multiplier method can handle complex constraint conditions and be applied to the simulation of explosive shock waves to establish highly reliable numerical simulation (NS) models. The finite element model can visually display the nonlinear forces and changes inside the analyzed object, making it very suitable for simulating the dynamic response of explosive shock wave impact helmets [5]. Therefore, the study adopts the Lagrange multiplier method to establish an NS model of explosion shock waves, and creates a finite element model of wearing a combat helmet on the head to analyze the defects of existing helmets under explosion impact, to improve the combat helmet. The research aims to combine these two methods to accurately simulate the protective performance of helmets under explosive impact, to determine specific measures to improve helmet protective performance.

The innovation of the study is the use of numerical simulation to optimize the design of the protective performance of the combat helmet, which breaks through the limitations of traditional experimental methods. Secondly, the study delves into the anisotropy and strain rate sensitivity of brain tissues, and incorporates these biomechanical properties into the finite element model to improve the biological realism of the model. By optimizing the shape, material distribution and cushioning foam structure of the helmet, this study proposes a novel design solution for combat helmets, which enhances the protective performance while taking into account the wearing comfort of the soldier and the lightweight requirement of the helmet. The design scheme not only provides a new idea for the design of military protective equipment, but also opens up a new direction for research in related fields.

The structure of the paper is as follows: Part 2 is a literature review summarizing the current state of the art in the application of numerical simulation techniques in the field of helmet optimization; part 3 describes the research methodology, including the establishment of numerical simulation models and optimization strategies; part 4 demonstrates the resultant analyses of the optimized helmet's protective performance; part 5 summarises the research results and suggests directions for future research.

2. Literature review

NST is widely used in various fields, which not only has the advantage of high-precision simulation, but also can save a lot of resource costs. Lagrange multiplier method and finite element model are two commonly used NS methods. With the development of technology, there are more and more studies using these two methods for NS. To solve the problem of excessive bubbles and impurities in steel continuous casting crystallizer operation, Lai et al. proposed an NS model based on Euler method and Lagrange multiplier method to simulate the liquid-solid-gas three-phase flow in the mold. This study demonstrates the potential application of numerical simulation in the field of materials processing and provides an effective method for the simulation of

complex flow fields [6]. Briney et al. used the unidirectional coupled Euler-Lagrange method to simulate the dynamic process of aircraft collision with snow and ice particles during supersonic flight and proposed an optimization method. This study provides new ideas and methods for the simulation of complex collision problems [7].

To solve the problem of difficult precise control of laser peen forming (LPF) technology for processing metal thin plates, Yong et al. established a finite element model (FEM) of metal characteristic strain and improved the LPF process. The results showed that after improving the LPF process, thin plates with a thickness of 4mm or less could be prepared [8]. In response to the problem of insufficient neck protection in police riot helmets during actual combat, Shi et al. used new materials and processes to optimize the helmets through experimental verification. The results showed that the new helmet improved the protective ability of personnel's head, face, and neck [9].

Combined with the above, it can be seen that numerical simulation technology has a wide range of application prospects in the field of protective equipment optimization. However, at present, the optimization of helmet protection capability mainly relies on traditional experimental verification methods. Therefore, an NS-based optimization method for combat helmets is proposed, aiming to conduct in-depth research on the protective performance of existing combat helmets, reveal their protective mechanisms and defects, and propose optimization design schemes.

3. Methodology

3.1. Analysis method for protective defects of existing combat helmets based on numerical simulation technology

NST can simulate the process of damage to soldiers' heads caused by explosion shock waves, including establishing models of explosion shock waves and models of soldiers wearing helmets on their heads, as well as the interaction between the two. Research can discover the defects of combat helmets from them [10,11]. There are many methods for NS, and previous research results have shown that the coupling of Lagrange algorithm and Euler algorithm is widely used in NS. This method combines the advantages of Euler algorithm in handling large deformations and Lagrange algorithm in simulating irregular or complex shapes. In addition, this coupling method can automatically shut down Euler flow field calculations, avoiding the problem of manually deleting explosive elements in pure Lagrangian calculations, thereby improving computational efficiency [12]. Coupling the Lagrangian and Eulerian algorithms and solving the complex shape and boundary conditions using the Lagrangian algorithm and the large deformation and fluid flow parts using the Eulerian algorithm during the simulation. Efficient simulation of complex problems is achieved by exchanging data and interactive calculations between the two. The problem of manually removing explosive elements in pure Lagrangian calculations is avoided by automatically switching off the Eulerian flow field calculations, which can improve the efficiency of the calculations. Therefore, the study introduces this coupling algorithm to model the blast shockwave using an arbitrary Lagrangian-Eulerian (ALE) formulation to deal with the motion and

deformation of the mesh. The basic form of the ALE formulation is shown in Equation (1).

$$\frac{\partial u}{\partial t} + (v \cdot \nabla)u = f \tag{1}$$

In Equation (1), u denotes the displacement field; v denotes the grid velocity; f denotes the external force; and t denotes time. The contact effect is simulated by calculating the interaction force between the meshes. The contact force is calculated as shown in Equation (2).

$$F_{contact} = k(\delta - \delta_0) + c\dot{\delta} \tag{2}$$

In Equation (2), k denotes the stiffness coefficient; δ denotes the actual distance between grids; δ_0 denotes the initial distance; c denotes the damping coefficient; and $\dot{\delta}$ denotes the rate of change of the distance. The coupling algorithm is introduced to model the explosion shock wave, and the schematic diagram of Lagrangian mesh deformation and algorithm cycle is denoted in **Figure 1**.

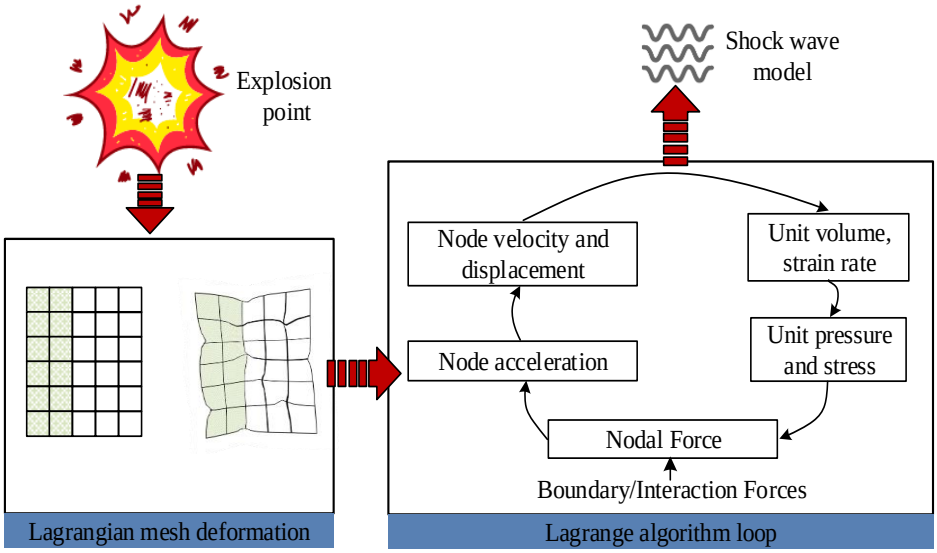

Figure 1. Lagrange mesh deformation and algorithm cycle diagram.

In **Figure 1**, when the explosion point generates an explosion shock wave, the air domain is divided into grids and undergoes deformation. The shock wave continuously circulates in the solid grid, achieving forward propagation. The calculation formula for the boundary force formed when the shock wave reaches the solid grid is shown in Equation (3).

$$\begin{cases} F_{x1} = \frac{1}{4}p[(y_E - y_Q)(z_D - z_Q) - (y_D - y_Q)(z_E - z_Q)] \\ F_{y1} = \frac{1}{4}p[(z_E - z_Q)(x_D - x_Q) - (z_D - z_Q)(x_E - x_Q)] \\ F_{z1} = \frac{1}{4}p[(x_E - x_Q)(y_D - y_Q) - (x_D - x_Q)(y_E - y_Q)] \end{cases} \tag{3}$$

In Equation (3), Q, D, E, and G are the four vertices of the solid mesh, p is the impact pressure, and F_{x1}, F_{y1}, and F_{z1} are the boundary forces. After obtaining the

boundary force, the acceleration calculation formula on the boundary is shown in Equation (4).

$$\ddot{x} = \frac{F_x}{m_p} + g_x, \ddot{y} = \frac{F_y}{m_p} + g_y, \ddot{z} = \frac{F_z}{m_p} + g_z \tag{4}$$

In Equation (4), m_p is the average quality of the eight units surrounding the node. g_x, g_y, and g_z denote the components of gravitational acceleration in three directions, while $\ddot{x}$, $\ddot{y}$, and $\ddot{z}$ are the components of acceleration in three directions. The calculation formula for obtaining the velocity and position of the node based on Equation (4) is shown in Equation (5).

$$\begin{cases} \dot{x}^{n+1/2} = \dot{x}^{n-1/2} + \ddot{x}^n \Delta t^n \\ x^{n+1} = x^n + \dot{x}^{n+1/2} \Delta t^{n+1/2} \\ x^{n+1/2} = \dfrac{1}{2}(x^{n+1} + x^n) \end{cases} \tag{5}$$

In Equation (5), $\dot{x}^{n+1/2}$ represents node speed, x^n and $x^{n+1/2}$ represent node positions, and Δt represents time step. After the deformation of the hexahedral solid mesh under impact, its volume is determined by the positions of 8 vertices, and the calculation formula for the volume is shown in Equation (6).

$$V = \int_0^1 \int_0^1 \int_0^1 \frac{\partial(x, y, z)}{\partial(\xi, \eta, \zeta)} d\ell d\eta d\zeta \tag{6}$$

In Equation (6), V is the unit volume, ℓ, η, and ζ are coordinate variables in the local coordinate system, d is the differential sign, and ∂ is the partial derivative. Equation (6) is in the form of volume integral, which can be converted into area fraction for further calculation of material flow velocity. The calculation formula for area fraction is shown in Equation (7).

$$\begin{cases} V = \dfrac{1}{3}\sum_{i,j} C_{ij} x_{ij}, i = 1,2,3; j = 1 \sim 8 \\ \int_0^V \dfrac{\partial f_i}{\partial x_i} dV = \int_0^S f_i \boldsymbol{n} \cdot ids \end{cases} \tag{7}$$

In Equation (7), n means the normal vector of the surface. C_{ij} is the stiffness matrix of the calculation unit, f_i is the force acting on the unit, and s is the boundary of the unit. The expression for the relationship between flow rate and volume change rate is shown in Equation (8).

$$\begin{cases} \dfrac{\dot{V}}{V} = \dot{\boldsymbol{\varepsilon}}_{xx} + \dot{\boldsymbol{\varepsilon}}_{yy} + \dot{\boldsymbol{\varepsilon}}_{zz} = \dfrac{\partial \dot{x}}{\partial x} + \dfrac{\partial \dot{y}}{\partial y} + \dfrac{\partial \dot{z}}{\partial z} \\ \dfrac{\partial \dot{x}}{\partial x} = \dfrac{1}{4V}\sum_{n=1}^{8} [\dot{x}_{AB}(\boldsymbol{A}_0 \times \boldsymbol{B}_0) \cdot i + \dot{x}_{CA}(\boldsymbol{C}_0 \times \boldsymbol{A}_0) \cdot i + \dot{x}_{BC}(\boldsymbol{B}_0 \times \boldsymbol{C}_0) \cdot i] \\ \dot{x}_{AB} = \dfrac{1}{3}(\dot{x}_1 + \dot{x}_2 + \dot{x}_4); \dot{x}_{CA} = \dfrac{1}{3}(\dot{x}_1 + \dot{x}_4 + \dot{x}_5); \dot{x}_{BC} = \dfrac{1}{3}(\dot{x}_1 + \dot{x}_2 + \dot{x}_5) \\ (\boldsymbol{A}_0 \times \boldsymbol{B}_0) \cdot i = (y_4 - y_1)(z_2 - z_1) - (y_2 - y_1)(z_4 - z_1) \\ (\boldsymbol{C}_0 \times \boldsymbol{A}_0) \cdot i = (y_5 - y_1)(z_4 - z_1) - (y_4 - y_1)(z_5 - z_1) \\ (\boldsymbol{B}_0 \times \boldsymbol{C}_0) \cdot i = (y_2 - y_1)(z_5 - z_1) - (y_5 - y_1)(z_2 - z_1) \end{cases} \tag{8}$$

In Equation (8), $\dot{\boldsymbol{\varepsilon}}_{xx}$, $\dot{\boldsymbol{\varepsilon}}_{yy}$, and $\dot{\boldsymbol{\varepsilon}}_{zz}$ indicate positive strains in three directions, respectively. $\boldsymbol{A}_0$, $\boldsymbol{B}_0$, and $\boldsymbol{C}_0$ are unit vertices. Afterwards, the deviatoric stress can be solved by combining the rotation correction $\boldsymbol{\delta}$, and the solution method is shown in Equation (9).

$$\begin{cases} \boldsymbol{s}_{xx}^{n+1} = \boldsymbol{s}_{xx}^{n} + 2G_a\Delta t[\dot{\boldsymbol{s}}_{xx} - \frac{1}{3}(\frac{\dot{V}}{V})]^{n+1/2} + \boldsymbol{\delta}_{xx}^{n} \\ \boldsymbol{s}_{yy}^{n+1} = \boldsymbol{s}_{yy}^{n} + 2G_a\Delta t[\dot{\boldsymbol{s}}_{yy} - \frac{1}{3}(\frac{\dot{V}}{V})]^{n+1/2} + \boldsymbol{\delta}_{yy}^{n} \\ \boldsymbol{s}_{zz}^{n+1} = \boldsymbol{s}_{zz}^{n} + 2G_a\Delta t[\dot{\boldsymbol{s}}_{zz} - \frac{1}{3}(\frac{\dot{V}}{V})]^{n+1/2} + \boldsymbol{\delta}_{zz}^{n} \\ \boldsymbol{s}_{xy}^{n+1} = \boldsymbol{s}_{xy}^{n} + 2G_a\Delta t\dot{\boldsymbol{\varepsilon}}_{xy}^{n+1/2} + \boldsymbol{\delta}_{xy}^{n} \\ \boldsymbol{s}_{yz}^{n+1} = \boldsymbol{s}_{yz}^{n} + 2G_a\Delta t\dot{\boldsymbol{s}}_{yz}^{n+1/2} + \boldsymbol{\delta}_{yz}^{n} \\ \boldsymbol{s}_{zx}^{n+1} = \boldsymbol{s}_{zx}^{n} + 2G_a\Delta t\dot{\boldsymbol{\varepsilon}}_{zx}^{n+1/2} + \boldsymbol{\delta}_{zx}^{n} \end{cases} \tag{9}$$

In Equation (9), ε is the degree of deformation of the material after being subjected to stress, G_a is the shear modulus, and $\boldsymbol{s}_{xx}^{n+1}$, $\boldsymbol{s}_{yy}^{n+1}$, $\boldsymbol{s}_{zz}^{n+1}$, $\boldsymbol{s}_{xy}^{n+1}$, $\boldsymbol{s}_{yz}^{n+1}$, and $\boldsymbol{s}_{zx}^{n+1}$ are the components of deviatoric stress. The new pressure is obtained by calculating the state equation, and the energy e^{n+1} calculation formula in the state equation is shown in Equation (10).

$$e^{n+1} = e^{n} + \Delta e^{n+1/2} - [\frac{p^{n+1} + p^{n}}{2} + q^{n+1/2}]\frac{\Delta V^{n+1}}{m} \tag{10}$$

In Equation (10), q is the viscous pressure. The calculation formula for the stress tensor of the new element after capturing the damping oscillation of the impact based on the viscous pressure is shown in Equation (11).

$$\boldsymbol{\sigma}_{xx} = -(p+q) + \boldsymbol{s}_{xx}, \boldsymbol{\sigma}_{yy} = -(p+q) + \boldsymbol{s}_{yy}, \boldsymbol{\sigma}_{zz} = -(p+q) + \boldsymbol{s}_{zz}, \\ \boldsymbol{\sigma}_{xy} = \boldsymbol{s}_{xy}, \boldsymbol{\sigma}_{yz} = \boldsymbol{s}_{yz}, \boldsymbol{\sigma}_{zx} = \boldsymbol{s}_{zx} \tag{11}$$

In Equation (11), $\boldsymbol{\sigma}$ represents stress. Based on stress, the motion of nodes in various directions can be obtained, and an FEM of explosion shock waves can be established using AUTODYN software. In order to ensure the accuracy and reliability of the model, the study made detailed reference to material parameters from authoritative biomechanical studies. According to Nahum's classical study, the material parameters of brain tissue are as follows: elastic modulus of 1.5 kPa, Poisson's ratio of 0.45, relaxation modulus of 0.8 kPa, and time constant of 0.1 s [13]. The skull material has a modulus of elasticity of 17 GPa, Poisson's ratio of 0.3 and a density of 1.85 g/cm^3. The scalp has a modulus of elasticity of 150 kPa, Poisson's ratio 0.4, and the meninges have a modulus of elasticity of 50 kPa, Poisson's ratio 0.35 [14]. The TNT explosives are modelled using 3D-Euler with a grid size of 5 mm. Considering the balance between the computational cost and the overall simulation accuracy, the grid size of 5 mm can better meet the research needs. The equations of state of air at different moments and the expressions of related parameters are shown in Equation (12).

$$\begin{cases} p = (\gamma - 1)\rho E/\rho_0 \\ p = A_1(1 - \frac{\omega}{R_1 V})e^{-R_1 V} + B_1(1 - \frac{\omega}{R_2 V})e^{-R_2 V} + \frac{\omega E_0}{V} \end{cases} \quad (12)$$

In Equation (12), E denotes the internal energy per unit volume of air, ρ_0 denotes the initial density of air, ρ denotes the density of air, γ denotes the specific heat ratio, and p is the air pressure. A_1, B_1, R_1, R_2, and ω are material parameters, and E_0 means the initial specific internal energy [15]. After establishing the models of explosion and shock wave, the research continued to create an FEM of wearing an ACH combat helmet on the head, analyzing the effect of the existing helmet under explosion impact. The schematic diagram of the simulation is denoted in **Figure 2**.

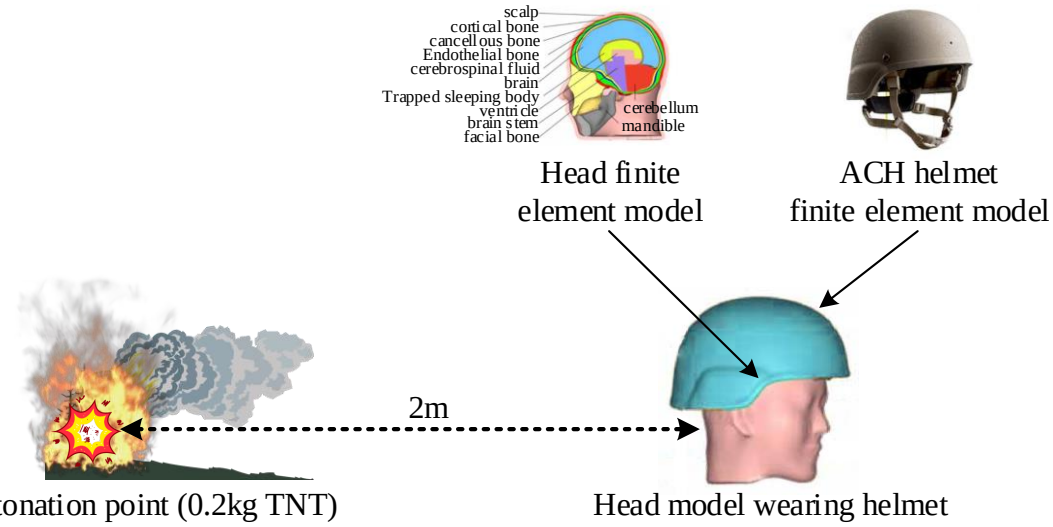

Figure 2. Simulation model of explosion shock wave acting on the head of soldiers wearing combat helmets.

In **Figure 2**, a model of explosion shock wave is established and combined with an FEM of the human brain to accurately predict the biomechanical response of the brain under the action of explosion shock wave. This provides a reliable tool for the mechanism of injury caused by explosion shock wave to the brain and the analysis of the protective effect of helmets on the brain [16,17]. In the finite element model, the interaction between the skull and the cerebrospinal fluid is realized by the fluid-structure interaction boundary condition. This coupling boundary condition can accurately simulate the interaction between the flow of cerebrospinal fluid and the movement of the skull, thus more realistically reflecting the dynamic response of the head under the action of the blast wave. On this basis, the anisotropic and strain rate sensitive properties of brain tissue were further analyzed. White and grey matter in brain tissue have different mechanical properties, and these properties show significant anisotropy in different directions. The study used Hill's criterion to characterise the anisotropic properties and the intrinsic relationship is shown in Equation (13) [18].

$$f(\sigma) = (\frac{\sigma_{11}}{E_1})^2 + (\frac{\sigma_{22}}{E_2})^2 + (\frac{\sigma_{33}}{E_3})^2 - 2v_{12}\frac{\sigma_{11}\sigma_{22}}{E_1 E_2} - 2v_{13}\frac{\sigma_{11}\sigma_{33}}{E_1 E_3} - 2v_{23}\frac{\sigma_{22}\sigma_{33}}{E_2 E_3} \leq 1 \quad (13)$$

In Equation (13), σ is the stress; E_1, E_2, and E_3 denote the modulus of elasticity in the three principal directions, respectively. v_{12}, v_{13}, and v_{23} denote Poisson's ratio. The anisotropy ratio of white matter is about 3:1, and the elastic modulus of grey matter is about 1.2 kPa, with a Poisson's ratio of 0.47. There are differences in the mechanical behaviors of brain tissues at different strain rates and are more important for simulating the dynamic response to an explosive shock wave. Therefore, the study was described using the Johnson-Cook model. Specifically, it is shown in Equation (14).

$$\sigma = A + B(\frac{\varepsilon}{\varepsilon_0})^n(1 + \frac{\dot{\varepsilon}}{\dot{\varepsilon}_0})^m \tag{14}$$

In Equation (14), A and B denote material constants. ε denotes strain, ε_0 denotes reference strain, $\dot{\varepsilon}$ denotes strain rate; $\dot{\varepsilon}_0$ denotes reference strain rate. n and m denote strain hardening index and strain rate hardening index. By introducing the strain rate sensitivity model, the dynamic response of the brain tissue under the effect of the blast shock wave can be more accurately simulated, thus better reflecting the damage mechanism of the brain tissue. Finally, the study simulated the situation of not wearing an ACH helmet and wearing an ACH helmet in the explosion shock wave, and the simulation data is shown in **Figure 3**.

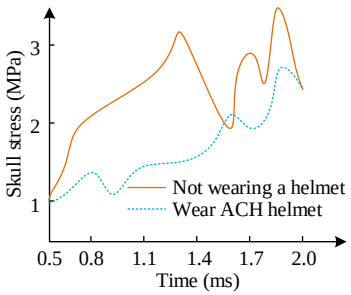

(a) Skull stress-time history curve.

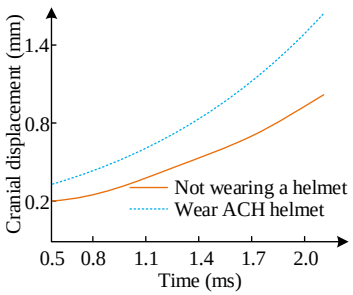

(b) Brain displacement-time history curve.

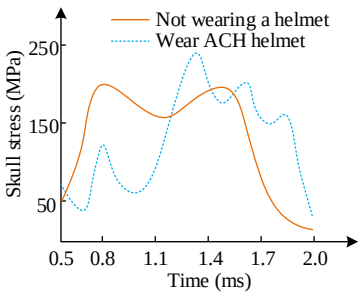

(c) Soft tissue pressure-time history curve.

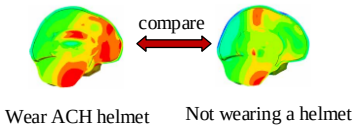

(d) Soft tissue pressure cloud map.

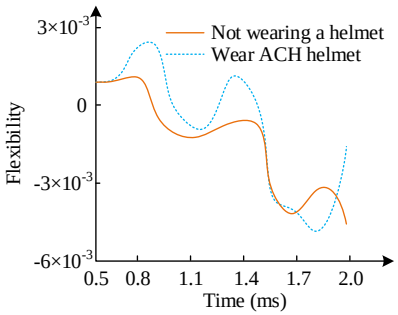

(e) Brain strain-time history curve.

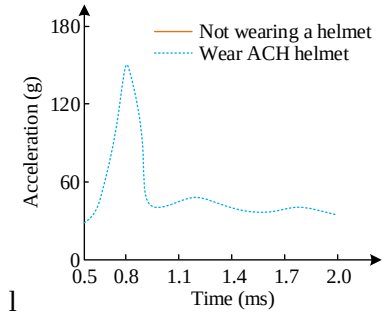

(f) Brain acceleration-time history curve.

Figure 3. Simulation data of wearing and not wearing helmets in explosion shock waves.

In **Figure 3a**, the rate of increase in skull stress without wearing a helmet was higher than that with a helmet, and the peak stress was higher. In **Figure 3b**, the peak displacement of the skull without a helmet was 0.92 mm, while the peak displacement of the skull with a helmet was 1.48 mm. The reason for the larger displacement of the skull with a helmet is that the shock wave repeatedly impacts the

head inside the helmet. In **Figure 3c**,**d**, when not wearing a helmet, the peak pressure of brain tissue was concentrated at the skull base, with a peak pressure of 188 kPa. After wearing the helmet, the damage area expanded to other parts, with a peak pressure of 235 kPa, exacerbating the traumatic brain injury. In **Figure 3e**, the two changes in the early stage of impact were consistent. However, in the middle and late stages, the peak strain of the brain with helmet protection was significantly higher than without helmet protection, indicating that the contraction and extension of the head under helmet protection are more significant. In **Figure 3f**, the overall acceleration of wearing a helmet was lower than that of not wearing a helmet, but the short-term acceleration within 1 ms was higher than that of not wearing a helmet. This high-speed vibration could cause brain injuries such as contusion and laceration.

3.2. Strategy for improving helmet protection performance to reduce the risk of head injury in the face of explosive shock waves

The results of NS showed that although wearing existing advanced combat helmets could resist direct injuries such as shrapnel, the presence of explosive shock waves could repeatedly impact the head inside the helmet, leading to more severe brain damage. To better protect soldiers' heads, further research is needed on new helmet materials and structural designs to enhance their protection against explosive shock waves. Based on the ACH combat helmet, the shape, material distribution and cushion foam structure were improved [19,20]. In terms of helmet shape, a fully covered helmet of the same mass as the ACH combat helmet was designed and studied, and the cross-section of the helmet is denoted in **Figure 4**.

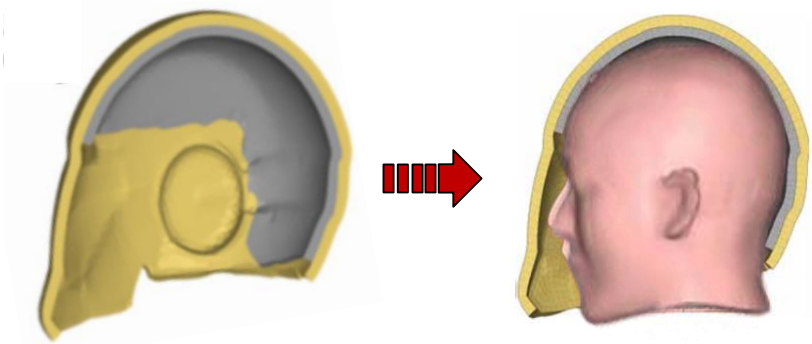

Figure 4. ACH combat helmet with full coverage and improved design.

In **Figure 4**, the fully covered helmet was designed inspired by the shape of a human skull, with a fully wrapped shape around the head. In order not to increase the burden of soldiers, the quality of the new helmet is the same as that of the ACH combat helmet. The helmet body thickness is reduced to 5.9 mm, while the cushion foam is not adjusted. When shock waves propagate in different media, both transmitted and reflected waves are generated, which can weaken the transmission of shock waves. Researching the use of this pattern to design the material distribution in helmets in order to reduce the impact of shock waves. The expression that shock

waves need to satisfy for continuous transmission in different media is shown in Equation (15).

$$\begin{cases}\sigma_r + \sigma_f = \sigma_t \\ v_r + v_f = v_t\end{cases} \tag{15}$$

In Equation (15), t denotes the transmitted wave, f denotes the reflected wave, r is the incident wave, v is the particle velocity. The expression for the discontinuous jump condition of stress waves in a medium is shown in Equation (16).

$$\begin{cases}d\sigma = \pm c\rho' dv \\ [\sigma] = \pm c\rho'[v]\end{cases} \tag{16}$$

In Equation (16), $\pm$represents the incident direction, ρ'denotes the density of the medium, and c denotes the velocity of the stress wave in the medium. It is assumed that wave impedance $c\rho' = \eta$, stress $c\rho' = \eta$. The transmitted stress wave of shock wave in two media is $\begin{cases}\boldsymbol{\sigma}_f = -\eta_1 v_f \\ \boldsymbol{\sigma}_t = \eta_2 v_t\end{cases}$, and $\frac{\sigma_r}{\eta_1} = \frac{\sigma_f}{\eta_1} + \frac{\sigma_t}{\eta_2}$ can be obtained according to Equation (15). Therefore, the expressions for the tansmitted wave in medium 2 and the reflected wave in medium 1 are shown in Equation (17).

$$\begin{cases}\sigma_f = -\dfrac{\eta_2 - \eta_1}{\eta_1 + \eta_2}\sigma_r \\ \sigma_t = \dfrac{2\eta_2}{\eta_1 + \eta_2}\sigma_r\end{cases} \tag{17}$$

In Equation (17), η_1 and η_2 are the wave impedances of two media. Similarly, the calculation formula for the transmitted wave stress when the shock wave is transmitted to medium 3 is shown in Equation (18).

$$\sigma_t = \frac{4\eta_2\eta_3}{(\eta_1 + \eta_2)(\eta_2 + \eta_3)}\sigma_r \tag{18}$$

In Equation (18), η_3 is the wave impedance of medium 3 [21]. Due to $\begin{cases}\boldsymbol{\sigma}_f = -\boldsymbol{\mu}_f \boldsymbol{\sigma}_r \\ \boldsymbol{\sigma}_t = \boldsymbol{\mu}_t \boldsymbol{\sigma}_r\end{cases}$, the stress wave reflection coefficient $\mu_f = (\eta_2 - \eta_1)/(\eta_1 + \eta_2)$ and stress wave transmission coefficient $\mu_t = 2\eta_2/(\eta_1 + \eta_2)$ can be calculated according to Equation (17). The formula for calculating the ratio n of the acoustic impedance of two media is shown in Equation (19).

$$n = \frac{\eta_1}{\eta_2} = \frac{(\rho_0 c_0)_1}{(\rho_0 c_0)_2} \tag{19}$$

In Equation (19), $(\rho_0 c_0)_1$ denotes the wave impedance of medium 1, and $(\rho_0 c_0)_2$ denotes the wave impedance of medium 2. From this, the wave impedance of the medium is an important factor affecting the propagation of shock waves [22]. Polyurea materials have strain rate effects and high energy absorption properties, and are biocompatible under normal conditions of use [23]. In addition, the change in performance of polyurea materials under extreme environmental conditions is an important factor in assessing their suitability. According to the relevant literature, polyurea materials show good stability in high and low temperature environments, but the toughness of polyurea materials may decrease in low temperature environments at −40 °C, while their hardness may increase in high temperature

environments at +60 °C [24,25]. Therefore, Polyurea materials exhibit strain rate effects and high energy absorption properties. The stress response expression of polyurea materials under different tensile ratios is shown in Equation (20).

$$\frac{t_1}{2\left(\lambda_1-\frac{1}{\lambda_1^2}\right)}=C_{aa}+\frac{1}{\lambda_1}C_{bb} \tag{20}$$

In Equation (20), C_{aa} and C_{bb} are the hyperelastic model parameters of the material. According to Equation (20), the stress of polyurea material increases with the increase of tensile ratio, and this increase is nonlinear [26]. Therefore, the study added polyurea material inside the ACH combat helmet to reduce the damage of shock waves to the brain. The distribution of polyurea materials is shown in **Figure 5**.

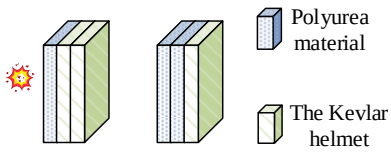

(a) Blast setting layer.

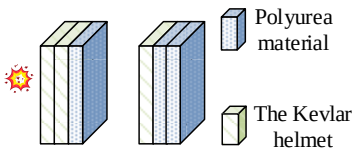

(b) Backburst layer.

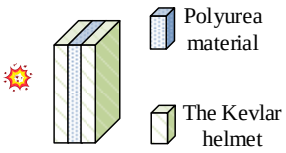

(c) Sandwich layer.

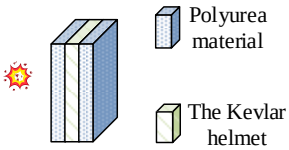

(d) Double layer polyurea material.

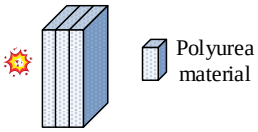

(e) All polyurea material layer.

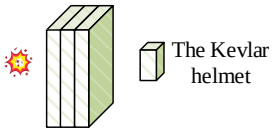

(f) Original.

Figure 5. Schematic diagram of distribution of polyurea materials.

In **Figure 5**, the arrangement of the polyurea layer can take various forms, including polyurea material as the blast layer, back layer, sandwich layer, or double-sided layer, as well as all using polyurea material. Based on the transmission properties of shock waves, the study selected a design with a double-sided polyurea layer and a Kevlar layer in between to maximize reflection and absorption, thereby reducing the risk of traumatic brain injury. Finally, in terms of liner foam structure, the pores in the perforated foam can reflect and diffract the shock wave, thereby absorbing energy. Through the finite element simulation, the energy absorption and deformation characteristics of foam with various porosity under the impact of explosion shock wave were compared and analyzed. The simulation analysis shows that the porosity of open cell foam has a significant impact on energy absorption. When the porosity is 15%, the foam has the largest deformation and the best energy absorption effect, which is 85% higher than that of closed cell foam. Therefore, the research designed the cushion foam of ACH combat helmet to randomly delete 15% of the grid volume in each layer. Finally, through the optimization design of the shape, polyurea material distribution and cushion foam structure of ACH combat

helmet, a soldier combat helmet with stronger anti shock wave destruction ability was obtained.

4. Result

To assess the shock wave protection performance of the newly designed ACH combat helmet, a series of experiments were conducted to analyze it. The experimental environment included simulation environment and verification experiment. The simulation environment used FEMs to numerically simulate the strain of the brain and combat helmet under the action of shock waves, to test the protective performance of the new ACH combat helmet without a physical helmet. The validation experiment was conducted using the Nahum cadaver head impact test, and the reliability of the FEM of the human head designed and constructed was verified through classical cadaver experiments.

4.1. Reliability verification of explosion shock wave model and finite element simulation of the head

To improve the existing ACH combat helmet, an NS model was established for the explosion shock wave, human head, and combat helmet. These models have a significant impact on the simulation accuracy of real situations and the optimization design of helmets. Therefore, experimental verification was conducted on the reliability of the explosion shock wave model and the finite element simulation of the head. The study compared the shock wave model established by Lagrange algorithm with the explosion shock wave model established by Sadovskyi, Henrych, Brode, and Cheng Q W empirical formulas. The test results are shown in **Figure 6**.

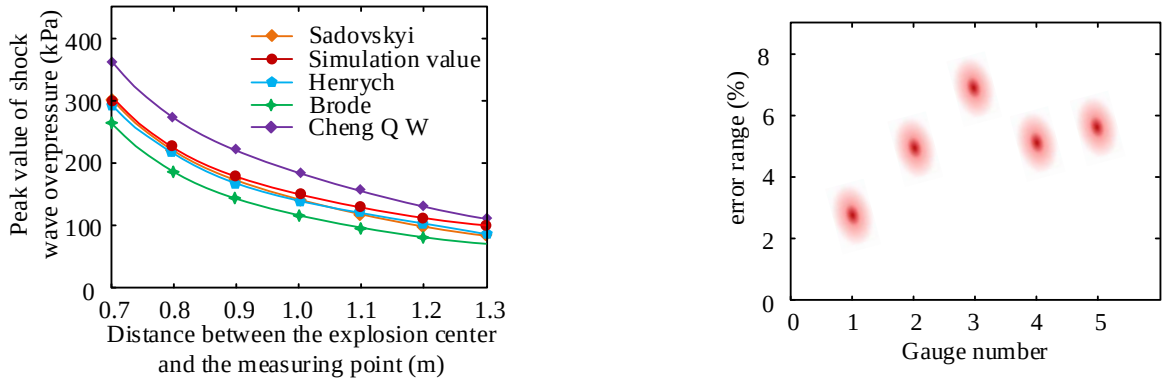

(a) Comparison between simulated values and empirical formulas.

(b) Error between 6 measuring points and theoretical peak value.

Figure 6. Verification of explosion shock wave model.

In **Figure 6a**, the simulation values for establishing the shock wave model were close to the four empirical value curves, indicating a high degree of consistency between the simulation solution and the theoretical solution. The peak value of shock wave overpressure in the simulation results was slightly higher than the empirical value, indicating that the simulation results are conservative. In **Figure 6b**, the average error between the pressure peak values at five measurement points in the established explosion shock wave model and empirical values was 5.1%. The results

indicated that the explosion shock wave model had high reliability and could be used for helmet optimization. To verify the reliability of the FEM of the head constructed in the study, Nahum cadaver head impact experiments were used for comparative verification. The comparison between the finite element simulation results of head impact and experimental data is shown in **Figure 7**.

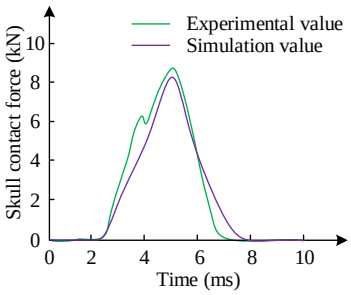

(a) Skull contact force curve.

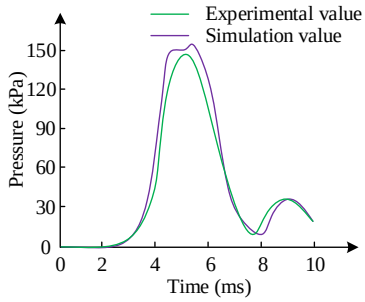

(b) Pressure value in the frontal bone area.

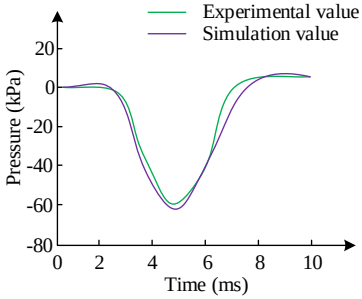

(c) Pressure value in the occipital region.

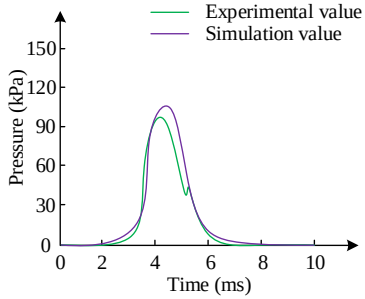

(d) Pressure value in the parietal region.

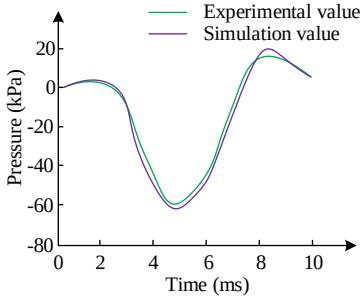

(e) Pressure values in the cerebellar fossa region.

Figure 7. Verification of finite element model of human head.

In **Figure 7a**, the skull contact force curve shows an error rate of 4.79% between the simulation results and the experimental results. In **Figure 7b**, the pressure curve of the frontal bone area shows an error rate of 3.91% between the simulation results and the experimental results. In **Figure 7c**, the pressure curve of the occipital region shows an error rate of 2.35% between the simulation results and the experimental results. In **Figure 7d**, the pressure curve in the parietal region shows an error rate of 3.17% between the simulation results and the experimental results. In **Figure 7e**, the pressure curve of the cerebellar fossa area shows an error rate of 2.65% between the simulation results and the experimental results. The results indicated that the human brain FEM had high sensitivity and was suitable for analyzing the mechanism of brain injury caused by explosive shock waves. On this basis, the study introduced the head model developed by the Kungliga Tekniska

Högskolan (KTH) in Sweden and the Global Human Body Models Consortium head model (GHBMC) for comparison with the proposed model. This is shown in **Table 1**.

Table 1. Results of statistical analyses.

Model type	Mean error (%)	*t*-test		ANOVA	
		t-value	*P*-value	*F*-value	*P*-value
Study proposed model	3.25	-	-	4.56	0.012
KTH	5.12	2.34	0.021**	-	-
GHBMC	4.87	1.98	0.045*	-	-

Note: * indicates that the difference is significant at $p < 0.05$; ** indicates that the difference is highly significant at $p < 0.01$.

As can be seen from **Table 1**, the mean error of the proposed head model is 3.25%, which is significantly lower than that of KTH and GHBMC. Analysis of Variance (ANOVA) shows an *F*-value of 4.56, which indicates that the difference in error between all three models is statistically significant. This further demonstrates the reliability and applicability of the proposed models of the study.

4.2. Performance analysis of optimized combat helmet protection

To verify the protective performance of the optimized combat helmet, relevant simulation tests were conducted. In the testing of the new full coverage helmet, the study chose to not wear a helmet, wear a traditional ACH helmet, wear an improved full coverage helmet with the same thickness as ACH, and compare it with the newly designed helmet to verify the brain injury situation under different helmet wearing conditions. The simulation results are shown in **Figure 8**.

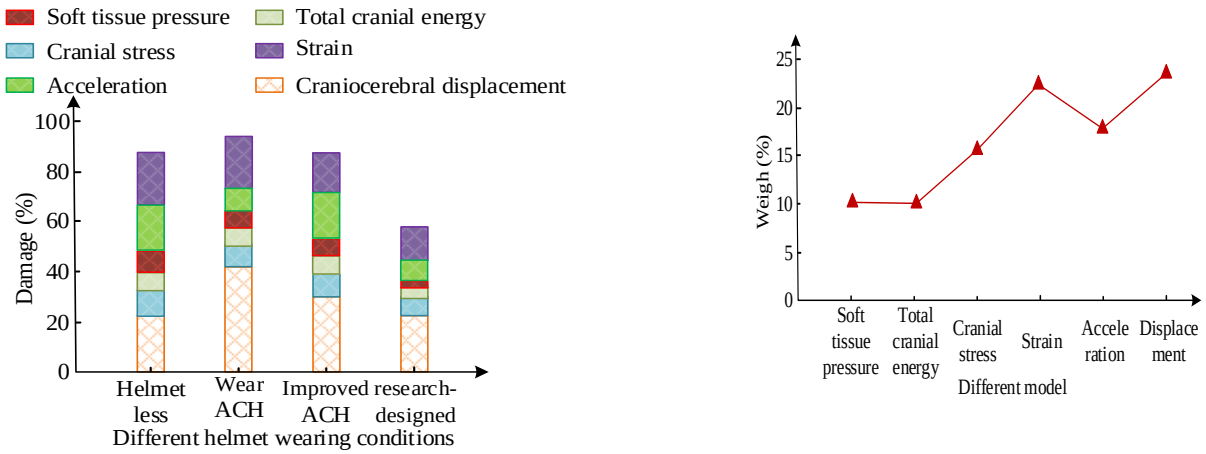

(a) Changes of craniocerebral injury under different helmet wearing conditions. **(b)** Weight of each evaluation index.

Figure 8. Analysis of full coverage helmet protection capability.

According to **Figure 8a**, wearing the new ACH helmet reduced the incidence of traumatic brain injury by 29.3%, 36%, and 29.2%, respectively, compared to not wearing a helmet, wearing a traditional ACH helmet, and wearing a fully covered improved helmet with the same thickness as ACH. According to **Figure 8b**, the weights of indicators for cranial acceleration, cranial strain, soft tissue pressure,

cranial displacement, cranial stress, and total cranial energy in various types of cranial injuries were 0.175, 0.221, 0.104, 0.237, 0.156, and 0.107, respectively. The outcomes denoted that the new helmet had stronger protection against shock waves compared to traditional ACH combat helmets. To verify the optimization effect of using a double-sided polyurea layer with a Kevlar layer sandwiched in between on ACH helmets, explosion shock wave damage tests were conducted on combat helmets with different polyurea layer arrangements. The simulation experiment outcomes are denoted in **Figure 9**.

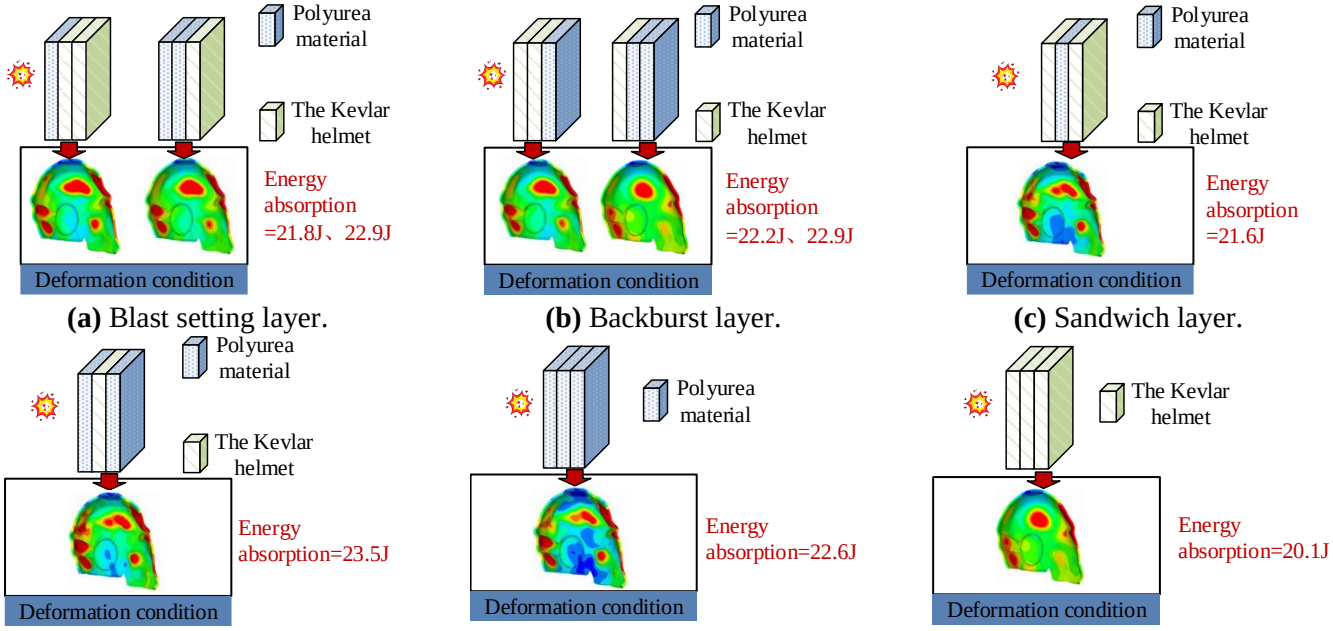

(a) Blast setting layer. **(b)** Backburst layer. **(c)** Sandwich layer.

(d) Double layer polyurea material. **(e)** All polyurea material layer. **(f)** Original.

Figure 9. Deformation of helmet with different arrangement of polyurea layer.

In **Figure 9a**, when polyurea material was used as the blast layer for the first and first two layers, the deformation of the helmet material was significant, and the absorption of shock wave energy was 21.8 J and 22.9 J, respectively. In **Figure 9b**, when polyurea material was used as the back layer of the last 1 or last 2 layers, the deformation was similar to that of the blast layer, with energy absorption of 22.2 J and 22.9 J, respectively. In **Figure 9c**, when polyurea material was used as the intermediate sandwich layer, the deformation was smaller than that of the blast layer and the back layer, and the shock wave energy absorption value was 21.6 J. In **Figure 9d**, when polyurea material was used as the inner and outer double-sided layer, the degree of deformation was the highest, and the shock wave energy absorption value was 23.5 J. In **Figure 9e**, when all three layers were made of polyurea material, the degree of deformation was between the blast resistant layer and the double-sided layer, and the shock wave energy absorption value was 22.6 J. In **Figure 9f**, when all three layers were Kevlar layers, the degree of deformation was the smallest, and the shock wave energy absorption value was 20.1 J. The results indicated that the double-sided layer designed in the study had the highest absorption value of shock wave energy, which could absorb more explosive shock wave energy than traditional ACH helmets, thereby reducing traumatic brain injury. To verify the

improvement effect of liner foam structure optimization on the protective ability, eight helmets with different porosity were used for comparison. The simulation results are shown in **Figure 10**.

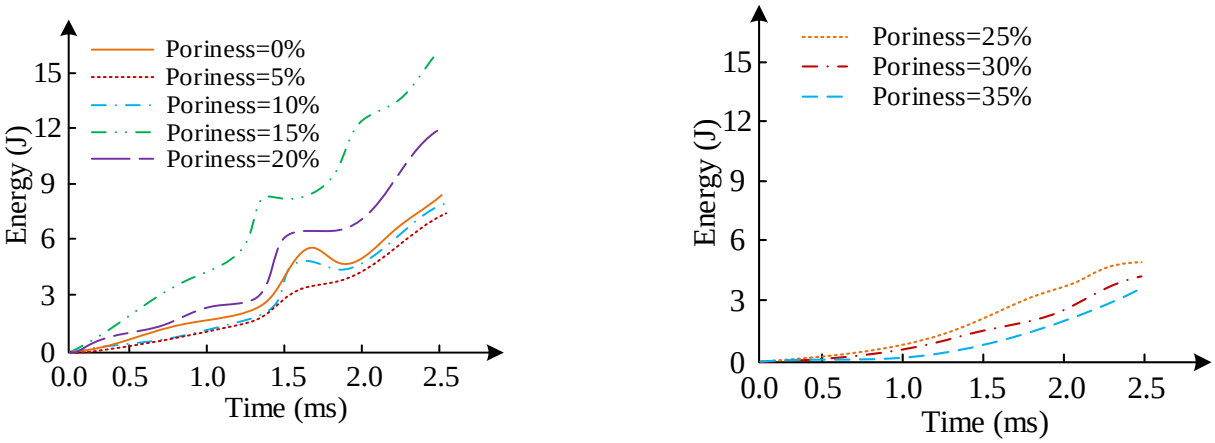

(a) The porosity is less than 20%. **(b)**The porosity is greater than 20%.

Figure 10. Energy absorption of foam with different porosity.

In **Figure 10a**, when the porosity was less than 20%, with the increase of the porosity, the change of the absorbed energy of the liner foam was nonlinear. When the porosity was 15%, the absorption effect of shock wave energy was the best. In **Figure 10b**, when the porosity was greater than 20%, the absorption effect of shock wave energy gradually decreased and the protective performance gradually decreased with the increase of porosity. Finally, the study further analyzed the biomechanical injury indicators of different helmets, as shown in **Table 2**.

Table 2. Comparison of biomechanical injuries under different helmet designs.

Helmet type	Von Mises stress (MPa)	Maximum principal strain	Brain strain rate (s^{-1})	Shear stress (Pa)
No helmet	2.3 ± 0.4	0.013 ± 0.003	135 ± 25	780 ± 120
Traditional ACH helmet	1.9 ± 0.3	0.007 ± 0.002	105 ± 18	560 ± 90
Improved full-coverage helme	1.6 ± 0.2	0.005 ± 0.002	90 ± 15	480 ± 80
New ACH helmet	1.4 ± 0.3	0.006 ± 0.003	110 ± 20	520 ± 100

From **Table 2**, it can be seen that the Von Mises stress of the new ACH helmet proposed in the study is only 1.4 MPa, and the maximum principal strain is 0.006, which is significantly lower than other helmet types. Shear stress is one of the important factors leading to brain tissue damage. When there is no helmet, the shear stress is highest, indicating that the head is subjected to significant shear force under impact. The traditional ACH helmet and the improved all inclusive helmet have optimized the pad structure and material distribution, reducing shear stress. The shear stress of the new ACH helmet proposed in the study is slightly higher than that of the improved fully wrapped helmet, which may be due to its design focus on overall energy absorption rather than simply reducing shear stress. Overall, the new ACH helmet proposed in the study has the lowest degree of biomechanical damage, indicating its best protective effect.

5. Practical application feasibility analysis

The study optimized the protective performance of the combat helmet through numerical simulation techniques to reduce the risk of head injury to soldiers from blast shock waves. The optimized combat helmet adopts polyurea material as the inner and outer face layers and combines Kevlar material as the middle layer. Polyurea materials are widely used in protective equipment due to their excellent energy absorption properties and strain rate effects. However, the production cost of polyurea materials is relatively high in mass production. The research will follow up by optimizing the thickness and distribution of the polyurea material to maintain high protective performance without increasing the cost. As for the manufacturing process, the optimized design of the helmet needs to consider the bonding technology between the polyurea layer and the Kevlar layer. The bonding strength between polyurea and Kevlar directly affects the overall performance and service life of the helmet. Relevant studies have shown that the use of automated hot compression moullding technology can shorten the production cycle by about 30%, thus increasing the feasibility of mass production [27]. This indicates that the optimal design method for helmets proposed in the study has positive application value.

6. Conclusions

The explosion shock wave causing brain injury to soldiers is a high-frequency phenomenon on the modern battlefield. The research aimed to analyze the dynamic response of soldiers' heads and helmets under the action of explosion shock waves through NS methods, reveal the protective mechanism and shortcomings of ACH combat helmets, and improve them to enhance the head protection capability of ACH combat helmets. The study used Lagrange algorithm to establish an NS model of explosion shock waves and established an FEM of wearing ACH combat helmets on the head. Then, by simulating the effect of shock wave on head injury, the shortcomings of ACH were identified, and the shape, material distribution and cushion foam structure of the helmet were optimized accordingly. The experimental results showed that wearing the new ACH helmet resulted in a 36% lower incidence of traumatic brain injury compared to wearing the traditional ACH helmet. When polyurea material was used as the inner and outer double-sided layer, the deformation degree of the helmet material was the highest, and the shock wave energy absorption value was 23.5 J. When the porosity was 15%, the absorption effect of shock wave energy was the best. The results show that the research-designed helmet optimization scheme effectively solves the limitations of traditional helmets in blast shock wave protection performance and reduces the risk of brain injury. This design not only improves the protection performance, but also takes into account the comfort and lightweight requirements, providing new ideas and directions for the design of military protective equipment. The numerical simulation technology adopted by the institute also provides technical support for the intelligent design and material innovation of future protective equipment, and promotes the

transformation of military protective equipment from traditional experimental verification to efficient and accurate digital design.

However, the study still has some shortcomings. The study mentions the model's simplification of the human brain and material properties as well as the limitation of computational resources to the simulation of complex battlefield environments. Future work will be devoted to enhancing model accuracy, improving materials and processes, reducing costs, and further improving helmet design through experimental validation to promote the intelligent and personalized development of military protective equipment.

Author contributions: Conceptualization, YS; methodology, YS; software, ZC; data curation, ZC; writing—original draft preparation, YS; writing—review and editing, ZC. All authors have read and agreed to the published version of the manuscript.

Ethical approval: Not applicable.

Conflict of interest: The authors declare no conflict of interest.

Abbreviations

ACH	Advanced Combat Helmet
LPF	Laser Peen Forming
FEM	Finite Element Model
KTH	Kungliga Tekniska Högskolan
GHBMC	Global Human Body Models Consortium head model
ANOVA	Analysis of Variance

References

1. Qu S, Meng C, Jin H, et al. A Design and Intelligent Recommendation Method for Ballistic Missile Early Warning Operation Plan. International journal of pattern recognition and artificial intelligence. 2023; 37(16): 1–21.
2. Andrushchenko VA, Goloveshkin VA, Murashkin IV, Kholin NN. Vortex Formation in the Frontal Zone Behind a Shock Wave of a Strong Point Explosion in an Inhomogeneous Atmosphere. High temperature: English translation of teplofizika vysokikh temperatur. 2022; 60(4): 578–581.
3. Wang L, Kong D, Shang F. Influence of homogeneous discontinuous medium on the propagation law of explosion shock wave pressure. Indian journal of physics and proceedings of the Indian Association for the Cultivation of Science. 2024; 98(3): 985–995.
4. Burman E, Hansbo P, Larson M. Cut finite element method for divergence-free approximation of incompressible flow: a lagrange multiplier approach. SIAM Journal on Numerical Analysis. 2024; 62(2): 893–918.
5. Wei J, Li C, Ma Y. Finite element model for static characteristic analysis of rolling linear guide. Proceedings of the Institution of Mechanical Engineers, Part C: Journal of Mechanical Engineering Science. 2022; 236(3): 1721–1732.
6. Lai Q, Luo Z, Zhang Y, et al. Numerical Simulation of Multiphase Flow in Steel Continuous Casting Mold Using a Novel Euler–Euler–Lagrange Method. Steel Research International. 2022; 93(9): 1–14.
7. Briney S, Balachandar S. Euler–Lagrange stochastic modeling of droplet breakup and impact in supersonic flight. Phys. Fluids. 2023; 35(1): 1–18.
8. Yong HL, Da XD, Xiu YXC. Investigation on the bending deformation of laser peen forming with a simplified eigenstrain-based finite element model. The International Journal of Advanced Manufacturing Technology. 2024; 131(12): 5815–5830.
9. Shi LF, Liu CM, Wang J, Wang HY. Analysis on Optimization and Improvement Technology of 2020Police Anti-Riot Helmet. Police Technology. 2022; 22(2): 54–59.

10. Rycman A, Bustamante M, Cronin DS. Brain Material Properties and Integration of Arachnoid Complex for Biofidelic Impact Response for Human Head Finite Element Model. Annals of biomedical engineering. 2024; 52(4): 908–919.
11. He G, Fan L, Horstemeyer MF. Embedded finite element modeling of the mechanics of brain axonal fiber tracts under head impact conditions. Computers in Biology and Medicine. 2024; 181(1): 1–6.
12. Zhang Y, Rong Y, Zheng H. A Study of Numerical Pollution of the Decoupled Algorithm for the Convection Model in Superposed Fluid and Porous Layers. SIAM Journal on Numerical Analysis. 2023; 61(2): 1018–1056.
13. Rey JA, Ewing JR, Sarntinoranont M. A computational model of glioma reveals opposing, stiffness-sensitive effects of leaky vasculature and tumor growth on tissue mechanical stress and porosity. Biomechanics and modeling in mechanobiology. 2021; 20(5): 1981–2000.
14. Walsh DR, Ross AM, Newport DT, et al. Mechanical characterisation of the human dura mater, falx cerebri and superior sagittal sinus. Acta biomaterialia. 2021; 134(10): 388–400.
15. Chilmeran HTS, Hamed ET, Al-Bayati AAY. A Method of Two New Augmented Lagrange Multiplier Versions for Solving Constrained Problems. International journal of mathematics and mathematical sciences. 2022; 2022(1): 1–6.
16. Rasheed AT, Biswas PP, Sreya MA. Effect of reciprocal headgear forces on the calvarium: A finite element study. American Journal of Orthodontics and Dentofacial Orthopedics. 2023; 163(3): 347–356.
17. Yu X, Wu T, Nguyen TTN, Ghajari M. Investigation of blast-induced cerebrospinal fluid cavitation: Insights from a simplified head surrogate. International Journal of Impact Engineering. 2022; 162(4): 1–9.
18. Zare Hosseinabadi S, Sabour MH, Fakoor M. Mixed-mode I/II criterion based on combining Hill failure analysis and reinforcement isotropic solid model. Acta Mechanica. 2023; 234(4): 1437–1450.
19. Breeze J, Fryer R N, Russell J. Comparing the medical coverage provided by four contemporary military combat helmets against penetrating traumatic brain injury. BMJ military health. 2022; 168(5): 395–398.
20. Huang X, Chang L, Zhao H, Cai Z. Study on craniocerebral dynamics response and helmet protective performance under the blast waves. Materials & Design. 2022; 224(1): 1–10.
21. Zhou F, Zhou Z, Ma Q. Study on the vibration isolation performance of an open trench–wave impedance block barrier using perfectly matched layer boundaries. Journal of Vibration and Control. 2022; 28(3): 329–338.
22. Wang L, Wu C, Fan L, Wang M. Effective velocity of reflected wave in rock mass with different wave impedances of normal incidence of stress wave. International journal for numerical and analytical methods in geomechanics. 2022; 46(9): 1607–1619.
23. Yang H, Yang Y, Li Y, et al. Extrinsic Conditions for the Occurrence and Characterizations of Self-Healing Polyurea Coatings for Improved Medical Device Reliability: A Mini Review. ACS omega. 2023; 8(30): 26650–26662.
24. Liu W, He Y, Leng J. Humidity-responsive shape memory polyurea with a high energy output based on reversible cross-linked networks. ACS Applied Materials & Interfaces. 2022; 15(1): 2163–2171.
25. Ou X, Zou X, Liu Q, et al. Recyclable, fire-resistant, superstrong, and reversible ionic polyurea-based adhesives. Chemistry of Materials. 2023; 35(3): 1218–1228.
26. Liang M, Zhou M, Lu LF. Synergistic effect of combined blast loads on UHMWPE fiber mesh reinforced polyurea composites. International journal of impact engineering. 2024; 183(1): 1–16.
27. Ozturk F, Cobanoglu M, Ece RE. Recent advancements in thermoplastic composite materials in aerospace industry. Journal of Thermoplastic Composite Materials. 2024; 37(9): 3084–3116.